Journal Pre-proof

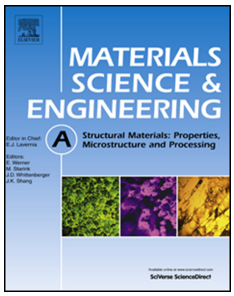

Microstructure and properties of equiatomic Ti–Ni alloy fabricated by selective laser melting

D.C. Ren, H.B. Zhang, Y.J. Liu, S.J. Li, W. Jin, R. Yang, L.C. Zhang

PII: S0921-5093(19)31372-3

DOI: https://doi.org/10.1016/j.msea.2019.138586

Reference: MSA 138586

To appear in: *Materials Science & Engineering A*

Received Date: 29 August 2019

Revised Date: 21 October 2019

Accepted Date: 23 October 2019

Please cite this article as: D.C. Ren, H.B. Zhang, Y.J. Liu, S.J. Li, W. Jin, R. Yang, L.C. Zhang, Microstructure and properties of equiatomic Ti–Ni alloy fabricated by selective laser melting, *Materials Science & Engineering A* (2019), doi: https://doi.org/10.1016/j.msea.2019.138586.

Microstructure and properties of equiatomic Ti-Ni alloy fabricated by selective laser melting

D.C. Ren [a, b], H.B Zhang [a, *], Y.J. Liu [a, *], S.J. Li [a], W. Jin [a], R. Yang [a], L.C. Zhang [c]

[a] *Institute of Metal Research, Chinese Academy of Sciences, Shenyang, 110016, China*

[b] *School of Materials Science and Engineering, University of Science and Technology of China, Shenyang, 110016, China*

[c] *School of Engineering, Edith Cowan University, Joondalup, Perth, WA 6027, Australia*

Abstract: Selective Laser Melting (SLM) as one of the additive manufacturing technologies can be used to produce Ti-Ni shape memory alloys with complex shape. In this work, equiatomic $Ti_{50}Ni_{50}$ (at.%) samples were produced by SLM with different scanning speed, and near-fully dense (99.5% relative density) parts were obtained under a low input laser energy density (40 J/mm^3) with the scanning speed of 1000 mm/s. The different scanning speeds had limited influence on the phase composition, transformation temperatures and Vickers hardness. Under low magnification, the typical molten pool morphology with inhomogenous microstructure was shown in the samples of SLM-produced Ti-Ni alloy, and self-accommodate martensite (B19′) twins with a few austenite (B2), nanoscale Ti_2Ni and rhombohedral (R) phases were found at higher magnification. Due to the formation of nanoscale Ti_2Ni phase and inhomogenous microstructure, the SLM-produced Ti-Ni alloy exhbited lower phase transformation temperatures and larger hysteresis temperatures between the start and finish point of the phase transformation compared to the starting used Ti-Ni powder. The formation of the R phase was contributed to the special repeat heating process and stress field formed by Ti_2Ni phase and dislocations in SLM equiatomic Ti-Ni alloy. The SLM-produced Ti-Ni alloy exhibits higher compressive and tensile fracture strength but lower compressive and tensile fracture strain compared to the conventional cast samples.

Keywords: selective laser melting; Ti-Ni; scanning speed; microstructures; mechanical properties

*Corresponding author. *E-mail address:* zhanghb@imr.ac.cn (H.B. Zhang),

liuyujing555@163.com (Y.J. Liu)

1. Introduction

Ti-Ni shape memory alloys have been widely used in medical and engineering fields for several decades due to their excellent performance such as shape memory and super-elasticity effect, biocompatibility with low elastic modulus, corrosion and fatigue resistance and high damping capacity [1-3]. In addition to the two common phases i.e. the high temperature mother phase of B2 and the low temperature of B19′ phase in Ti-Ni alloys, an intermediate R phase can also be observed during the transformation between B2 and B19′ [4-8]. In the near equiatomic Ti-Ni alloys, the phase transformation temperatures can shift by 10 ºC with the variation of 0.1 at.% Ni content, so it is possible to adjust the phase transformation temperatures between the two phases by manipulating the ratio of Ti and Ni elements or alloying other elements for different applications at various temperatures and environments [9-12]. However, the super-elasticity and shape memory effect can also make Ti-Ni alloys difficult to be machined for the resistance to deformation, and burrs can easily form on the sample surface when the cutting and feed speeds are not high enough [13]. Such a drawback limits the applications of this type of alloy in to the forms of simple rods, plates and wires [13, 14]. In addition to the traditional cast method, powder metallurgy (such as self-propagating high temperature synthesis, hot isostatic pressing, and spark plasma sintering) as the net shape fabrication method can also be used to fabricate the complex shape of Ti-Ni samples [15-17]. However, the content of brittle oxide impurities can be significantly increased from powder metallurgy process and it is hard to produce samples with a high relative density because of the different diffusivity between Ti and Ni and high exothermic during Ti-Ni formation reaction [13].

Recently, the additive manufacturing (AM) techniques including Selective Laser Melting (SLM) and Electron Beam Melting (EBM) have been used to fabricate industrialized complex geometry products [18-21]. In particular, customized porous structure metal implants have elastic modules close to that of human bones, which can closely cover the surface of solid parts, provide space for bone tissue growth for better

fixation [22-24]. AM technology can reduce oxidation during manufacturing and obtain near-fully dense samples by melting and solidifying the powder via layer-by-layer in an inert gas or vacuum environment. Using the AM technology combined with the shape memory effect of Ti-Ni alloy, the spatial and time-dependent functional response of the Ti-Ni shape memory alloy prepared by AM can be modulated by adjusting the AM process parameters, from which the concept of 4D printing can be realized [23, 25].

Due to their important applications in biomedical devices and industrial fields, Ti-Ni samples fabricated by AM techniques have been extensively investigated [2, 25-29]. For example, Marettukalam et al. [2] showed that the laser power and scanning speed could significantly affect the phase constituents, microstructure and corrosion resistance of laser engineered net shaping (LENS) produced Ti-Ni alloy. Ma et al. [25] studied the impact of SLM processing protocol on location-dependent thermal histories. Saedi et al. [26] found that aging heat treatment had a strongly influence on adjusting the shape memory properties and super-elasticity of SLM-produced Ni-rich Ti-Ni alloy. Haberland et al. [27] investigated the influence of processing parameters on the microstructure, defects and functional properties of AM Ti-Ni parts. Shiva et al. [29] successfully fabricated three different compositions Ti-Ni shape memory alloys used the laser based AM process and found the properties of Ni-50% Ti-50% (wt.%) were close to that of conventionally processed samples. However, most literature focused on the effects of AM processing parameters on the mechanical or functional properties of the Ti-rich or Ni-rich Ti-Ni products.

In this work, SLM was used to fabricate $Ti_{50}Ni_{50}$ (at.%) shape memory alloy, the influence of scanning speed (input laser energy density) on the relative density and defects was studied with aim to optimize the SLM processing parameters for Ti-Ni alloys. Then the microstructure, phase transformation temperatures, compressive mechanical property and the formation of precipitation phases in the SLM samples fabricated by optimal parameter were investigated in detail.

2. Experimental

The nominal composition of the $Ti_{50}Ni_{50}$ (at.%) hot rolled rods, produced with 45 mm in diameter and 600 mm in length by Institute of Metal Research (Chinese Academy of Sciences), were prepared into powder by gas atomization technique. The morphology of the powder (Fig. 1a) suggests that the powder is nearly spherical in shape. The distribution of particle size of the powder (Fig. 1b), which was measured by laser scattering particle size distribution analyzer (HORIBA LA-920), indicates that the powder has an average particle size of 35 μm, and such specific values are d_{10} = 19.6 μm, d_{50} = 34.79 μm, d_{90} = 54.75 μm (the *dx* representatives the particle size of the powder when the cumulative volume percent reaches the *x* value).

Several samples with different relative density were prepared using the Realizer SLM250 machine under a high-purity Argon with flow rate of 35 L/h to minimize oxidation. This machine was equipped with a 200 W Yb:YAG fiber laser for a spot size of 40 μm to melt the Ti-Ni powder. Cubic samples with an edge length of 8 mm were produced using laser scanning speeds varied from 500 to 2000 mm/s. The layer thickness and scan spacing were kept constant at 50 μm and 100 μm, respectively. Samples were built in 3 mm stripes with an alternating scanning strategy without overlap, the scanning vectors were rotated 90º between adjacent layers. Several selected sample groups (hereafter termed as SLM-500, SLM-750, SLM-1000, SLM-1500 and SLM-2000, respectively) were built at 500, 750, 1000, 1500 and 2000 mm/s, respectively. The density of the SLM samples was measured by the Archimedes principle and then the relative density of SLM-produced Ti-Ni samples were estimated from the percentage compared with the density (6.45 g/cm^3) of Ti-Ni cast sample.

The microstructural analysis was performed using a Tescan Maia3 scanning electron microscope (SEM) and a Tecnai G^2 F20 transmission electron microscope (TEM) equipped with an energy dispersive X-ray spectroscopy (EDS) detector. The specimens for the SEM analysis were mechanically polished and then etched in a solution composed of 10 vol.% HF, 30 vol.% HNO_3 and 60 vol.% H_2O for 30 s. The TEM specimens were prepared by a Leica RE S101 focused ion beam machining under accelerating voltage 5 kV and accelerating current 5 mA. Phase constitutions

were examined on a D/Max-2500PC 2D X-ray diffraction (XRD) using a Cu-Kα radiation source with an accelerating voltage of 40 kV and a current of 250 mA at a step size of 0.02º.

The phase transformation temperatures were performed using a TA Q20 Differential Scanning Calorimeter (DSC) instrument with heating and cooling rates of 10 ºC/min. The phase transformation temperatures between the low temperature phase B19′ and high temperature phase B2 as M_s (martensite start), M_p (martensite peak), M_f (martensite finish), A_s (austenite start), A_p (austenite peak) and A_f (austenite finish) were determined by the intersecting tangents method. The Vickers hardness tests were conducted using a LM-247AT Vickers hardness tester with a 0.2 kg load and a dwell time of 15 s. A total of 10 measurements on each sample were performed. The compressive testing was carried out using an INSTRON 5582 universal testing machine according to ASTM E9 standard at room temperature at a strain rate of 1.0×10^{-3} s^{-1}. The tensile samples fabricated by the same parameters with SLM-1000 and the experiment were performed at room temperature using a Zwick/Z150 testing machine equipped with a MakroXtens automatic extensometer, and samples fabricated according to ASTM E9 standard with a constant beam displacement rate of 1 mm/minute.

3. Results

3.1 Processing optimization

Fig. 2 displays the relative density of the studied SLM-produced Ti-Ni samples fabricated by different scanning speed and input laser energy density. For all the studied SLM-produced samples, their relative density has reached above 90%. For the parameters, the relative density does not show a linear relationship with scanning speed increasing or input laser energy density decreasing. When the scanning speed is 1000 mm/s as the input laser energy density is 40 J/mm^3, the relative density of the sample reaches the maximum value of 99.5%. It is important to mention that the input laser energy density is much lower than the values reported in literature for getting high relative density beyond than 99% for the SLM-produced Ti-Ni parts (e.g. 200

J/mm^3) and for SLM-produced Ti alloys (e.g. 120 J/mm^3) [27, 30].

The effect of scanning speed on the defects type of SLM-produced Ti-Ni samples is shown in Fig. 3. When the scanning speed is higher than 1000 mm/s, the relative density decreases with increasing the scanning speed (Fig. 2). In this case, the defects are mainly the lack-of-fusion porosities with un-melted powder filled inside. As shown in Fig. 3a, the defects usually have an irregularly shape. When the scanning speed is lower than 1000 mm/s, the relative density reduces with the decrease in scanning speed (Fig. 2). The type of defects can be the gas porosities, which have a nearly spherical shape, and/or cracks, as displayed in Fig. 3b. It can also be detected that the gas porosities are much smaller in size than the lack-of-fusion-porosities.

3.2 Phase identification and transformation

The XRD spectra of the SLM-produced Ti-Ni parts fabricated by different scanning speeds and Ti-Ni powder are presented in Fig. 4. It is seen that the SLM-produced samples mainly consist of B19′ and Ti_2Ni phase. Unlike the Ti-Ni powder, small amount of B2 phase with weak peak intensity (~42.8º peak) is also detected in all the SLM-produced samples with different scanning speeds, for B2 phase can be stabilized to room temperature due to the fast cooling rate during solidification [28]. The same peak positions can be found in all the SLM-produced Ti-Ni samples fabricated in different scanning speed and the original Ti-Ni powder. Most of the stronger intensity peaks (e.g. the peaks around ~39.2º, 41.4º and 45.2º) are overlapped and the intensity of other weaker peaks are too little (e.g. the peaks around ~ 60.1º and 66.2º) to select, so it is restricted to calculate the relative amounts of the two phases of B19′ and Ti_2Ni using the XRD technique described in literature to investigate the influence of the scanning speed or input laser energy density to the phase contents [31].

The phase transformation behaviors of the original powder and the SLM-produced parts fabricated by different scanning speeds are shown in Fig. 5. The corresponding transformation temperatures are summarized in Table 1. It seems that only one endothermic peak and one exothermic peak are observed during the cooling

and heating processes (Fig. 5a), but the hysteresis temperatures between the start and finish point of the phase transformation of the SLM-produced samples are much larger than the corresponding ones of the powder. Furthermore, as seen from Fig. 5a and Table 1, all the transformation temperatures are close for the SLM-produced Ti-Ni samples fabricated by different scanning speeds. For example, the martensite transformation peak temperature M_p (42.5±2.5 ºC) and austenite transformation peak temperature A_p (75.5±3 ºC) are nearly the same (Fig. 5b). It is also interesting to find that the phase transformation temperatures for the studied SLM-produced samples are lower than the corresponding ones (e.g. M_p and A_p are 57.6 ºC and 96.9 ºC respectively) of original Ti-Ni powder, for most reported that the phase transformation temperatures larger than the initial powder or raw material [23, 27].

3.3 Microstructure

The SEM microstructure of the SLM-1000 sample is shown in Fig. 6. A typical molten pool morphology is observed under a low magnification (Fig. 6a). However, it can be observed at higher magnification that the molten pool is composed of the following different types of microstructural feature due to different cooling rates throughout the whole molten pool: the columnar grains grown vertical or even extend through the boundary of molten pool (Fig. 6b of the area of A in Fig. 6a), large scale equiaxed grains in the core region (Fig. 6c of the area of B in Fig. 6a), small sized equiaxed grains at the sub-boundary (Fig. 6d of the area of C in Fig. 6a) and nanoscale or sub-micron equiaxed grains near the boundaries of the molten pool (Fig. 6e of the area of D in Fig. 6a). A large number of precipitates with smaller diameter size of nanoscale are also observed most along the grain boundaries near the molten pool boundary, which make the boundaries of the molten pool form a sharp contrast with other areas (Fig. 6f).

A low-magnification scanning transmission electron microscopy (STEM) image for a grain boundary with precipitated phases is displayed in Fig. 7. It can be clearly seen that several precipitation phases with nanoscale are distributed along the grain boundary (Fig. 7a). The EDS results obtained from a precipitation at the grain

boundary shown in Fig. 7b and 7c indicate the particle consists of Ti and Ni elements, and their relative atomic contents are 64.40 and 35.60 respectively. The ratio of Ti contents to Ni contents is nearly 2:1, which suggests that these nanoscale particles in SLM-produced Ti-Ni sample should be Ti_2Ni phase.

Fig. 8 shows the TEM images and the corresponding selected area electron diffraction (SAED) patterns for the twins in the SLM-1000 sample. It is observed that the sample mainly consists of self-accommodated transformation lamellar B19′ phase at room temperature (Fig. 8a). The B19′ phase has band twinned structure with straight interfaces (Fig. 8b) and the thickness of each twin band is about ~10 nm. In general, there are usually three types of B19′ twins, such as {11-1} type I, {011} type II and {001} compound twins, in the near equiatomic Ti-Ni alloy. In this work, the corresponding SAED pattern obtained from the region containing twins (Fig. 8c) indicates that the twins in the SLM-1000 sample are the {011} type II with a misorientation angle of 145º at the twin boundaries (Fig. 8d) [32, 33].

3.4 Mechanical properties

The Vickers hardness results of the studied SLM-produced Ti-Ni samples are shown in Fig. 9. It can be found that there is only a slight fluctuation of hardness for 255±10 $HV_{0.2}$ with scanning speeds changed from 500 mm/s to 2000 mm/s (Fig. 9a). It can also be observed that the average hardness of SLM-1000 sample on the building direction (from bottom to top), 253±19 $HV_{0.2}$, and along the sample top surface, 251±24 $HV_{0.2}$, are very close (Fig. 9b). The reason for such a slight fluctuation in hardness is likely a result of the particular distribution of coarse and fine grains in the SLM fabricated samples [34].

The compressive and tensile stress-strain curves of SLM-1000 sample and conventional cast sample for the same $Ti_{50}Ni_{50}$ (at.%) composition are shown in Fig. 10. It can be seen that the SLM and cast samples present a very similar mechanical behavior. A typical double yielding behavior is observed and the whole compressive curve can be divided into four stages, i.e. the elastic deformation of martensite (or austensite), detwinning of martensite or reorientation, elastic deformation of

reoriented martensite and plastic deformation of reoriented martensite [35]. The SLM-1000 sample exhibits ~50 MPa higher compressive fracture stress and ~16 MPa higher tensile fracture stress than the cast counterpart. However, SLM-1000 sample ~2.2% compressive fracture strain and ~1.9% tensile fracture strain lower than the cast sample. The compressive fracture stress is about ~2200 MPa larger than the reported LENS Ni55.2 (wt.%) Ti-Ni shape memory alloy with the similar ~255 HV [28], and also about ~1800 MPa larger than the same $Ti_{50}Ni_{50}$ (at.%) alloy fabricated by plasma arc deposition method [8].

The difference in compressive and tensile mechanical properties (Fig. 10) between the SLM-1000 and the cast samples may be attributed to the difference in microstructure (Fig. 6). During the SLM process, huge residual stress is retained in the SLM-produced sample because of the high cooling rate, which can assist the martensite transformation [23]. Then, the process of martensite reorientation finished and the high density of dislocations and refinement microstructure introduced by the SLM process may lead to the higher fracture strength and lower fracture strain for the SLM-1000 samples [11, 23, 36].

The fracture morphologies of SLM-1000 after compressive testing are displayed in Fig. 11. The fracture takes place with an angle of 45º (Fig. 11a) aligned to the loading direction, which is in the maximum shear stress direction for compression, which has similar fracture direction with other reported SLM shape memory alloy [11]. The fracture surface along fracture direction is smooth (Fig. 11b), and no cracks are observed between the adjacent hatches of the SLM (Fig.11c). Dimple-like structure is not found at the magnified surface morphologies shown in Fig. 11d, which illustrates that the compressive fracture process is in the typically shear fracture mode.

4. Discussion

4.1 The effect of scanning speed

During SLM process, input laser energy density is an important factor to impact the density and defect. Generally, the relative density of SLM-produced part increases with the increase in the input laser energy density [37]. The input laser energy density

of SLM process is calculated using Equation (1) [26]:

$$E = \frac{P}{vhd} \quad (1)$$

where *E, P, v, h* and *d* are the input laser energy density (J/mm^3), laser power (W), scanning speed (mm/s), hatch spacing (mm), and layer thickness (mm), respectively. In this work, only scanning speed was designated to change input laser energy density for manipulation of the relative density of SLM-produced Ti-Ni alloy. For the Ti-Ni powder with particle size of 15~60 μm, the parameters set-up (*P* = 200 W, *v* = 1000 mm/s, *h* = 100 μm, *d* = 50 μm) with the lower input laser energy density of 40 J/mm^3 is the optimal processing parameters to fabricate nearly dense equiatomic $Ti_{50}Ni_{50}$ (at.%) alloy.

The laser absorption, radiation, reflection and heat transfer between liquid and solid phase etc. in the "laser radiation-powder-substrate" system could introduce various undesirable effects with the SLM processing parameters adjusted [38]. Additionally, different mechanics, powder types, scanning path and particle size, which have been reported in literature, can make the discrepancy for the required input laser energy density in producing dense parts of the same type of material [25]. So, the above reasons could cause the non-linear relationship between the scanning speed with the relative density and lower input laser energy density in fabricating nearly dense equiatomic $Ti_{50}Ni_{50}$ (at.%) alloy as shown in Fig. 2.

There are several types of defects inside the SLM-produced samples, as the processing parameters are not properly optimized. When the scanning speed exceed than the optimal scanning speed, the Ti-Ni powder would not have enough energy to melt sufficiently during the fabricating process, thereby leading to lack-of-fusion porosities with un-melted powder filled inside (Fig. 3a) and/or decreased relative density of samples (Fig. 2) [37, 38]. If the SLM parameters are not changed as the number of powder layer increases, the existing lack-of-fusion porosities would be coated inside the samples and new ones could randomly appear in anywhere. When the scanning speed is lower than the optimal speed as the input laser energy density is exceed the optimal density, the defects type becomes the gas porosities and cracks

(Fig. 3b). Since nearly spherical shape gas porosity is usually introduced by entrapment gas pre-existed in the Ti-Ni powder, powder feed system and metal vaporization for larger input laser energy density under the rapid melting progress [39, 40]. Furthermore, during the SLM process, the cooling rate could exceed 10^7 K/s, which can lead to a huge thermal gradient and residual stress between molten powder with relatively cold substrate or previously solidified layers [41]. Such a huge residual stress can be saved in SLM-produced parts to cause cracks (Fig. 3b) [23]. It is important to understand the types of defects generated under different SLM parameters and to choose the correct scanning speed to obtain Ti-Ni solid parts with the smallest defects.

The hardness of Ti-Ni alloy is highly dependent on the temperature as phase transformation could occur during the hardness testing, it refers to the process of stress-induced phase transformation of B2 to B19′ (or R) or reorientation of different B19′ twins variant [26]. It can be found that there is only a slight fluctuation of hardness (Fig. 9a), when testing in the same room temperature for the SLM-produced Ti-Ni samples fabricated with different scanning speeds. It can also be seen that the phase transformation temperatures prepared at different scanning speed are very close (Fig. 5). This may be due to the following reasons. Firstly, it is shown in Fig. 2 and Fig. 3 that the changing of the scanning speed has obvious influence on the density and defect types of the alloy sample. However, all the samples were fabricated in the same batch, with the same parameters for the print chamber environment, sample size and powder layer thickness, so the content of impurities such as oxygen and nitrogen in the samples will be the same, and the microstructure (Fig. 6) and composition of all the well fusion regions can be kept stable. Secondly, in order to decrease the effect on the properties of AM Ti-Ni alloys, the process parameters should be carefully manipulated in such a principle that the input energy density should be as low as possible for fabricating dense parts [27]. And it was reported that, when the input energy density was lower than 90 J/mm^3 with low laser power, the Ni evaporation could be negligible [42]. The input laser energy density displayed in Fig. 2 was changed from 20~80 J/mm^3 as the scanning speed changed from 500~2000 mm/s, and

all the value were lower than 90 J/mm^3, so the element contention for Ni and Ti in the samples fabricated in different scanning speed may changeless. Thirdly, It is important to note that when the Ni at.% content lower than 50 at.%, the phase transformation temperatures are almost constant [43, 44]. In this study, the powder is equiatomic $Ti_{50}Ni_{50}$ (at.%) used to fabricate the dense sample, so if considered the little negligible evaporation of Ni element, the Ni content in the SLM-produced Ti-Ni samples will lower than 50 at.%. In summary, the phase transformation temperatures are changeless with the changing of the scanning speed and stable in the room temperature for the hardness testing. Therefore, combined with the results of DSC (Fig. 5) and hardness testing results (Fig. 9), we can confirm that the SLM scanning speed also has limited influence on the relative amounts for the equiatomic $Ti_{50}Ni_{50}$ (at.%) alloy in this work.

4.2 Formation of Ti_2Ni phase

It is noted that, in this work, a large amount of Ti_2Ni phase in nanoscale is formed mainly along grain boundaries in the SLM-produced samples (Fig. 6). During the SLM process, the powder is rapidly heated above the melting point and the evaporation of alloying element from the molten pool would take place due to the high energy input from the laser in a short time [23]. As the boiling point of Ni (3186 K) is lower than that of Ti (3560 K), the equilibrium vapor pressure of Ti is much lower than Ni, which may lead to evaporation of Ni [23, 25, 26]. Since the heating and cooling rates are fast enough to suppress element diffusion to obtain chemical homogenization, the evaporation of Ni may cause the enrichment of Ti along the grain boundaries, especially in the molten pool boundary areas (Fig. 6). According to the Ti-Ni binary phase diagram, the Ti_2Ni reaction temperature (1257 K) is lower than that of Ti-Ni phase (1583 K), and the Ti_2Ni phase can be formed as the following reaction **[9]**:

$$2Ti + Ni = Ti_2Ni \quad (2)$$

The Gibbs free energy of reaction (2) is -78.03 kJ/mol, which indicates that it is a spontaneous reaction during the SLM fabrication process [9, 45].

The Ti_2Ni phase presents various morphologies in different type of Ti-Ni alloy. It was reported that in the Ti-rich Ti-Ni alloy, the microstructure primarily comprises columnar dendritic structures with 5~60 μm in size, along with the Ti_2Ni present the inter-dendritic regions [42, 45]. The size and morphology of the dendritic structure and Ti_2Ni phase can be manipulated by the laser energy density in the Ti-rich Ti-Ni alloy [42]. In the near equiatomic Ti-Ni alloys, Ti_2Ni precipitates with large aspect ratio can be observed in the Ti-Ni matrix [46]. According to the Ti-Ni phase diagram, the Ti_2Ni is mainly formed in the Ti-rich or near equiatomic Ti-Ni alloys. However, because of the formation kinetics is very fast for Ti_2Ni phase and oxygen stabilization or composition gradients formed during SLM process, the Ti_2Ni precipitates with 10~20 nm in size are also observed in the Ni-rich Ti-Ni alloy [25]. In this work, the studied alloy is equiatomic Ti-Ni. Unlike the reported alloys, the morphology of Ti_2Ni precipitates is partile-like in this work. This phenomenon may be attributed to the relatively low laser energy density used in this work to rapidly form the kinetics of the Ti-Ni phase, and the atomic fraction of the elements is almost equal. The formation of Ti_2Ni precipitates may affect the performance of the SLM-produced Ti-Ni alloy.

It has been widely reported that because of the evaporation of nickel during the SLM process, the phase transformation temperatures are higher than the original Ti-Ni powder [23, 27]. It is interesting that the corresponding phase transformation temperatures are lower than those of original Ti-Ni powder in this work and the hysteresis temperatures between the start and finish point of the phase transformation of SLM-produced samples are much larger than the corresponding ones of the powder (Fig. 5). The transformation temperatures of Ti-Ni alloys are very sensitive to microstructure (dislocations or precipitations) [23]. And the reason for such an abnormal phenomenon is attributed to the formation of Ti-rich secondary phases, such as Ti_2Ni phase precipitates (Fig. 6 and Fig. 7) formed by eutectoid reaction between Ti and Ni as discussed above. The influence of formation of Ti-rich precipitates may overcome the effect of the evaporation of Ni, thereby resulting in the decrease in transformation temperatures [14]. The un-homogeneous microstructure (Fig. 6) would cause the uneven element distribution in the Ti-Ni matrix, thereby resulting in much

larger hysteresis temperatures between the start and finish point of the phase transformation of SLM-produced samples than of the powder (Fig. 5) [10, 23].

4.3 Formation of R phase

It has been reported that for equiatomic Ti-Ni alloy, prepared using traditional methods, has a tendency to exhibit an R phase between the high and low temperature phases after thermal cycling [4, 12]. Thus, the B2 to B19′ transformation becomes the two-stage transformation after several thermal cycling. The first stage is from B2 to R, and the second is R to B19′. With the increase in thermal cycles, the R phase is stabilized [4]. During the SLM process, the previous layers are re-melted and re-heated several times until the manufacturing process is completed, which could be equivalent to a special constant thermal cycle, and it is also possible to form the R phase during repeated melting and heating.

As such, TEM observations were used to verify the existence of R phase in the SLM-produced equiatomic Ti-Ni alloy for sample of SLM-1000 in Fig. 12. It is interesting to observe that the diffraction spots located at near 1/3 position in the reciprocal lattice are very sharp and strong, which confirms the existence of R phase in the right and left regions of the grain boundary at room temperature in the B2 phase areas (Fig. 12a, 12b and 12c) [5, 6]. However, the content of the R phase is too less to be detected in the XRD pattern (Fig. 4) and DSC curves (Fig. 5). Some nonascale Ti_2Ni particles are also observed along the grain boundary (Fig. 12a). These results indicate that B19′, B2, R and Ti_2Ni phase coexist in the SLM-produced $Ti_{50}Ni_{50}$ (at.%) samples at room temperature. In addition, the repeating process could also introduce much lattice defects, such as dislocations (Fig. 12d), in the SLM-produced samples. The dislocations and embedded grain boundary Ti_2Ni particles in Ti-Ni matrix phase may create local stress fields, which may also accelerate B2 to R and suppress B2 to B19′ transformation [4, 8]. Consequently, the formation of R phase during the SLM processing was discussed above, but the effect of the R phase on properties of the SLM-produced Ti-Ni alloy also need to be investigated in the future.

5. Conclusion

In the work, the solid parts of equiatomic $Ti_{50}Ni_{50}$ (at.%) alloy were successfully fabricated by SLM, and the microstructure, phase transformation temperatures, compressive mechanical property and the formation of precipitation phases were investigated. The results are summarized as:

(1) The scanning speed of 1000 mm/s (thus with energy density of 40 J/mm^3) is the optimal parameter to achieve the dense product with the minimum defects. Lower or higher than this scanning speed, the density of SLM-produced equiatomic Ti-Ni samples decreases due to the formation of different types of defects,

(2) The phase composition, transformation temperatures and the Vickers hardness are changeless with the changing scanning speed .

(3) The SLM-produced equiatomic Ti-Ni samples mainly consist of self-accommodate <011> type II martensite (B19′) twins. The B2, R and Ti_2Ni phases are also detected in the samples.

(4) The formation of Ti_2Ni phase results in lower corresponding phase transformation temperatures for SLM-produced equiatomic Ti-Ni alloy than for the original Ti-Ni powder.

(5) Becaues of the special repeated heating process and stress field formed by Ti_2Ni phase and dislocations, the intermediate R phase is formed during the SLM process.

(6) Compared to the traditinal cast counterparts, the SLM-1000 samples exhibit higher compressive and tensile fracture stress with lower compressive and tensile strain.

Acknowledgments

The authors acknowledge partial support by the Strategic Priority Research Program of the Chinese Academy of Sciences (Grant No. XDA22010103), National Key Research and Development Program of China (2017YFC1104903, 2016YFC1102601), National Natural Science Foundation of China (51871220), Key Research Program of Frontier Sciences, CAS (QYZDJ-SSW-JSC031-02).

Reference

[1] G.B. Cho, K.W. Kim, H.J. Ahn, K.K. Cho, T.H. Nam, Applications of Ti–Ni alloys for secondary batteries, J. Alloys. Compd. 449 (2008) 317-321, https://doi.org/10.1016/j.jallcom.2006.01.129

[2] J.J. Marettukalam, A.K. Singh, S. Datta, M. Das, V.K. Balla, S. Bontha, S.K. Kalpathy, Microstructure and corrosion behavior of laser processed NiTi alloy, Mater. Sci. Eng. C. 57 (2015) 309-313, https://doi.org/10.1016/j.msec.2015.07.067

[3] T. Duerig, A. Pelton, D. Stöckel, An overview of nitinol medical applications, Mater. Sci. Eng. A. 273-275 (1999) 149-160, https://doi.org/10.1016/S0921-5093(99)00294-4

[4] H. Matsumoto, Transformation behavior of NiTi in relation to thermal cycling and deformation, Phy. B. 190 (1993) 115-120, https://doi.org/10.1016/0921-4526(93)90454-E

[5] D.T. Zhang, B. Guo, Y.X. Tong, B. Tian, L. Li, Y.F. Zhang, D.V. Gunderov, R.Z. Valiev, Effect of annealing temperature on martensitic transformation of Ti49.2Ni50.8 alloy processed by equal channel angular pressing, Trans. Nonferrous Met. Soc. China. 26 (2016) 448-455, https://doi.org/10.1016/S1003-6326(16)64133-X

[6] Z.G. Wang, X.T. Zu, X.D. Feng, S. Zhu, J.M. Zhou, L.M. Wang, Annealing-induced evolution of transformation characteristics in TiNi shape memory alloys, Phy. B. 353 (2004) 9-14, https://doi.org/10.1016/j.physb.2004.08.021

[7] M. Elahinia, N.S. Moghaddam, M.T. Andani, A. Amerinatanzi, B.A. Bimber, R.F. Hamilton, Fabrication of NiTi through additive manufacturing: a review, Prog. Mater. Sci. 83 (2016) 630-663, https://doi.org/10.1016/j.pmatsci.2016.08.001

[8] B.W. Lu, X.F. Cui, E.B. Liu, X.R. Feng, M.L. Dong, Y. Li, H.D. Wang, G. Jin, Influence of microstructure on phase transformation behavior and mechanical properties of plasma arc deposited shape memory alloy, Mater. Sci. Eng. A. 736 (2018) 130-136 https://doi.org/10.1016/j.msea.2018.08.098

[9] B.C. Zhang, J. Chen, C. Codder, Microstructure and transformation behavior of in-situ shape memory alloys by selective laser melting Ti-Ni mixed powder, J. Mater. Sci. Technol. 29 (2013) 863-867, https://doi.org/10.1016/j.jmst.2013.05.006

[10] M. Speirs, X. Wang, S.V. Baelen, A. Ahadi, S. Dadbakhsh, On the transformation behavior of NiTi shape-memory alloy produced by SLM, Shap. Mem. Superelasticity. 2 (2016) 310-316, https://doi.org/10.1007/s40830-016-0083-y

[11] P. Gargarella, C.S. Kiminami, E.M. Mazzer, R.D. Cava, L.A. Basilio, C. Bolfarini, W.J. Botta, J. Eckert, T. Gustmann, S. Pauly, Phase formation, thermal stability and mechanical properties of a Cu-Al-Ni-Mn shape memory alloy prepared by selective laser melting, Mat. Res. 18 (2015) 35-38, http://dx.doi.org/10.1590/1516-1439.338914

[12] L.Q. Wang, L.C. Xie, L.C. Zhang, L.Y. Chen, Z.H. Ding, Y.T. Lv, W. Zhang, W.J. Lu, D. Zhang, Microstructure evolution and superelasticity of layer-like NiTiNb porous metal prepared by eutectic reaction, Acta Mater. 143 (2018) 214-226, https://doi.org/10.1016/j.actamat.2017.10.021

[13] M.H. Elahinia, M. Hashemi, M. Tabesh, S.B. Bhaduri, Manufacturing and processing of NiTi implants: A review, Prog. Mater. Sci. 57 (2012) 911-946, https://doi.org/10.1016/j.pmatsci.2011.11.001

[14] N.S. Moghaddam, S.E. Saghaian, A. Amerinatanzi, H. Ibrahim, P.Z. Li, G.P. Toker, H.E. Karace, M. Elahinia, Anisotropic tensile and actuation properties of NiTi fabricated with selective laser melting, Mater. Sci. Eng. A. 724 (2018) 220-230, https://doi.org/10.1016/j.msea.2018.03.072

[15] C. Zanotti, P. Giuliani, A. Terrosu, S. Gennari, F. Maglia, Porous Ni–Ti ignition and combustion synthesis, Intermetallics. 15 (2007) 404-412, https://doi.org/10.1016/j.intermet.2006.08.002

[16] A.S. Jabur, J.T. Al-Haiday, E.S. Al-Hasani, Characterization of Ni–Ti shape memory alloys prepared by powder metallurgy, J. Alloys. Compd. 578 (2013) 136-142, https://doi.org/10.1016/j.jallcom.2013.05.029

[17] Y. Zhao, M. Taya, Y.S. Kang, A. Kawasaki, Compression behavior of porous NiTi shape memory alloy, Acta Mater. 53 (2005) 337-343, https://doi.org/10.1016/j.actamat.2004.09.029

[18] Y.J. Liu, S.J. Li, H.L. Wang, W.T. Hou, Y.L. Hao, R. Yang, T.B. Sercombe, L.C. Zhang, Microstructure, defects and mechanical behavior of beta-type titanium porous structures manufactured by electron beam melting and selective laser melting, Acta Mater. 113 (2016) 56-67, https://doi.org/10.1016/j.actamat.2016.04.029

[19] Y.J. Liu, S.J. Li, L.C. Zhang, Y.L. Hao, T.B. Sercombe, Early plastic deformation behaviour and energy absorption in porous beta-type biomedical titanium produced by selective laser melting, Scripta Mater. 153

(2018) 99-103, https://doi. 10.1016/j.scriptamat.2018.05.010

[20] L.C. Zhang, Y.J. Liu, S.J. Li, Y.L. Hao, Additive manufacturing of titanium alloys by electron beam melting: A Review, Adv. Eng. Mater. 20 (2018) 1700842, https://doi.org/10.1002/adem.201700842

[21] L.C. Zhang, D. Klemm, J. Eckert, Y.L. Hao, T.B. Sercombe, Manufacture by selective laser melting and mechanical behavior of a biomedical Ti-24Nb-4Zr-8Sn alloy, Scripta Mater. 65 (2011) 21-24, https://doi.org/10.1016/j.scriptamat.2011.03.024

[22] X.L. Zhao, S.J. Li, M. Zhang, Y.D. Liu, T.B. Sercombe, S.G. Wang, Y.L. Hao, R. Yang, L.E. Murr, Comparison of the microstructures and mechanical properties of Ti–6Al–4V fabricated by selective laser melting and electron beam melting, Mater. Des. 95 (2016) 21–31, https://doi.org/10.1016/j.matdes.2015.12.135

[23] X.B. Wang, S. Kustor, J.V. Humbeeck, A short review on the microstructure, transformation behavior and functional properties of NiTi shape memory alloys fabricated by selective laser melting, Materials. 11 (2018) 1683, https://doi.org/10.3390/ma11091683

[24] D.C. Ren, S.J. Li, H. Wang, W.T. Hou, Y.L. Hao, W. Jin, R. Yang, R.D.K. Misra, L.E. Murr, Fatigue behavior of Ti-6Al-4V cellular structures fabricated by additive manufacturing technique, J. Mater. Sci. Technol. 35 (2019) 285-294, https://doi.org/10.1016/j.jmst.2018.09.066

[25] J. Ma, B. Franco, G. Tapia, K. Karayagiz, L. Johnson, J. Liu, R. Arroyave. I. Karaman, A. Elwany, Spatial control of functional response in 4D-Printed active metallic structures, Sci. Rep. 7 (2017) 46707, https://doi.org/10.1038/srep46707

[26] S. Saedi, A.S. Turabi, M.T. Andani, C. Haberland, H. Karaca, M. Elahinia, The influence of heat treatment on the thermomechanical response of Ni-rich NiTi alloys manufactured by selective laser melting, J. Alloys. Compd. 677 (2016) 204-210, https://doi.org/10.1016/j.jallcom.2016.03.161

[27] C. Haberland, M. Elabinia, J.M. Walker, H. Meier, On the development of high quality NiTi shape memory and pseudoelastic parts by additive manufacturing, Smart. Mater. Struct. 23 (2014) 104002, https://doi.10.1088/0964-1726/23/10/104002

[28] B.V. Krishna, S. Bose, A. Bandyopadhyay, Laser processing of net-shape NiTi shape memory alloy, A. Metall. Mat. Trans. A. 38 (2007) 1096-1103, https://doi.org/10.1007/s11661-007-9127-4

[29] S. Shiva, I.A. Palani, S.K. Mishra, C.P. Paul, L.M. Kukreja, Investigations on the influence of composition in the development of Ni-Ti shape memory alloy using laser based additive manufacturing, Opt. Laser. Technol. 69 (2015) 44-51, https://doi. 10.1016/j.optlastec.2014.12.014

[30] L.C. Zhang, H. Attar, Selective laser melting of titanium alloys and titanium matrix composites for biomedical applications: A review, Adv. Eng. Mater. 18 (2016) 463-475, https://doi.org/10.1002/adem.201500419

[31] S.J. Li, R. Yang, M. Niinomi, Y.L. Hao, Y. Y. Cui, Z.X. Guo, Phase transformation during aging and resulting mechanical properties of two Ti–Nb–Ta–Zr alloys, Mater. Sci. Technol. 21 (2005) 678- 686, https://doi.org/10.1179/174328405X43108

[32] Z.L. Xie, Y. Liu, J.V. Humbeeck, Microstructure of NiTi shape memory alloy due to tension-compression cyclic deformation, Acta Mater. 46 (1998) 1989-2000, https://doi.org/10.1016/S1359-6454(97)00379-0

[33] G. Tadayyon, M. Mazinani, Y. Guo, S.M. Zebarjad, S.A.M. Tofail, M.J. Biggs, The effect of annealing on the mechanical properties and microstructural evolution of Ti-rich NiTi shape memory alloy, Mater. Sci. Eng. A. 662 (2016) 564-577, https://doi.org/10.1016/j.msea.2016.03.004

[34] C.L. Yang, Z.J. Zhang, S.J. LI, Y.J. Liu, T.B. Sercombe, W.T. Hou, P. Zhang, Y.K. Zhu, Y.L. Hao, Z.F. Zhang, R. Yang, Simultaneous improvement in strength and plasticity of Ti-24Nb-4Zr-8Sn manufactured by selective laser melting, Mater. Des. 157 (2018) 52-59, https://doi.org/10.1016/j.matdes.2018.07.036

[35] S.Y. Jiang, Y.Q. Zhang, Microstructure evolution and deformation behavior of as-cast NiTi shape memory alloy under compression, Trans. Nonferrous Met. Soc. China. 22 (2012) 90-96, https://doi.org/10.1016/S1003-6326(11)61145-X

[36] L.F. Liu, Q.Q. Ding, Y. Zhong, J. Zou, J. Wu, Y.L. Chiu, J.X. Li, Z. Zhang, Q. Yu, Z.J. Shen, Dislocation network in additive manufactured steel breaks strength–ductility trade-off, Mater. Today. 21 (2018) 354-361, https://doi.org/10.1016/j.mattod.2017.11.004

[37] D.D. Gu, Y. C. Hagedorn, W. Meiners, G.B. Meng, R.J.S. Batista, K. Wissenbach, R. Poprawe, Densification behavior, microstructure evolution, and wear performance of selective laser melting processed commercially pure titanium, Acta Mater. 60 (2012) 3849-2860, https://doi.org/10.1016/j.actamat.2012.04.006

[38] H. Attar, M. Calin, L.C. Zhang, S. Scudino, J.Eckert, Manufacture by selective laser melting and mechanical behavior of commercially pure titanium, Mater. Sci. Eng. A. 593 (2014) 170-177, https://doi.org/10.1016/j.msea.2013.11.038

[39] C.H. Song, Y.Q. Yang, Y.D. Wang, D. Wang, J.K. Yu, Research on rapid manufacturing of CoCrMo alloy femoral component based on selective laser melting, Int. J. Adv. Manuf. Technol. 75 (2014) 445-453, https://doi.org/10.1007/s00170-014-6150-7

[40] C.L. Qiu, C. Panwisawas, M. Ward, H.C. Basoalto, J.W. Brooks, M.M. Attallah, On the role of melt flow into the surface structure and porosity development during selective laser melting, Acta Mater. 96 (2015) 72-79,

https://doi.org/10.1016/j.actamat.2015.06.004

[41] Y.J. Liu, Z. Liu, Y. Jiang, G.W. Wang, Y. Yang, L.C. Zhang, Gradient in microstructure and mechanical property of selective laser melted AlSi10Mg, J. Alloys. Compd. 735 (2018) 1414-1421, https://doi.org/10.1016/j.jallcom.2017.11.020

[42] C.L. Tan, S. Li, K. Essa, P. Jamshidi, K.S. Zhou, W.Y. Ma, M.M. Attallah, Laser powder bed fusion of Ti-rich TiNi lattice structures: process optimisation, geometrical integrity, and phase transformations, Int. J. Mach. Tool. Manu. 141 (2019) 19-29, https://doi.org/10.1016/j.ijmachtools.2019.04.002

[43] W. Tang, B. Sundman, R. Sandstron, C. Qiu, New modelling of the B2 phase and its associated martensitic transformation in the Ti-Ni system, Acta Mater. 47 (1999) 3457-3468, https://doi.10.1016/S1359-6454(99)00193-7

[44] J. Frenzel, E.P. George, A. Dlouhy, C. Somsen, M.F.X. Wagner, G. Eggeler, Influence of Ni on martensitic phase transformations in NiTi shape memory alloys, Acta Mater. 58 (2010) 3444-3458, https://doi.10.1016/j.actamat.2010.02.019

[45] S. Li, H. Hassanin, M.M. Attallah, N.J.E. Adkins, K. Essa, The development of TiNi-based negative Poisson's ratio structure using selective laser melting, Acta Mater. 105 (2016) 75-83, https://doi.10.1016/j.actamat.2015.12.017

[46] H.L. Hou, E. Simsek, D. Stasak, N. Al Hasan, S.X. Qian, R. Ott, J. Cui, I. Takeuchi, Elastocaloric cooling of additive manufactured shape memory alloys with large latent heat, J. Phys. D: Appl. Phys. 50 (2017) 404001, https://doi.org/10.1088/1361-6463/aa85bf

Tables

Table 1

Phase transformation temperatures of SLM Ti-Ni parts and original Ti-Ni powder from DSC graphs

Sample	M_f / ºC	M_p / ºC	M_s / ºC	A_s / ºC	A_p / ºC	A_f / ºC
Powder	47.8	57.6	65.3	82.5	96.9	103.0
SLM-500	18.2	44.9	62.2	56.8	78.5	89.2
SLM-750	2.3	42.0	63.9	53.8	76.3	92.7
SLM-1000	7.4	42.4	64.4	51.0	74.4	93.5
SLM-1500	20.0	43.0	56.2	54.6	75.7	88.5
SLM-2000	13.5	40.2	60.2	50.0	73.4	87.6

Figure Captions

Fig. 1 (a) The SEM shape morphology and (b) the size distribution of Ti-Ni powder.

Fig. 2 The relationship between relative density of SLM Ti-Ni parts with SLM scanning speeds or input laser energy density.

Fig. 3 The SEM images for top surface after mechanically ground and polished to show the defects of (a) SLM-1500 and (b) SLM-500.

Fig. 4 The XRD spectra of the Ti-Ni powder and SLM fabricated samples at different laser scanning speeds.

Fig. 5 (a) The DSC curves and (b) temperature of phase transformation peaks of Ti-Ni powder and SLM fabricated samples at different laser scanning speeds.

Fig. 6 The SEM microstructure of SLM-1000: (a) top surface of molten pool, (b) the area of A in Fig. 6a for columnar grains, (c) the area of B in Fig. 6a for large scale equiaxed grains,, (d) the area of C in Fig. 6a for little size equiaxed grains, (e) the area of D in Fig. 6a for nanoscal or sub-micro equiaxed grains, (f) molten pool boundary area.

Fig.7 (a) Low-magnification STEM image of a grain boundary with precipitation phases in SLM-1000, (b) and (c) EDS results obtained from a precipitation marked in (a).

Fig. 8 TEM microstructure of SLM-1000: (a) bright field image, (b) the morphology of twins, (c) the corresponding SAED pattern obtained from the region containing twins, (d) high-resolution TEM image for a twin with the misorientation angle of 145° at the twin boundaries.

Fig. 9 The Vickers hardness of (a) SLM fabricated samples in different scanning speed and (b)

SLM-1000 along the building direction and the top surface on a straight testing line that spans the entire sample for ten different positions respectively.

Fig. 10 The compression of (a) and tensile of (b) stress-strain curves loaded until failure for SLM-1000 and the cast counterpart with the same chemical composition.

Fig. 11 (a) The morphology of SLM-1000 before and after compression testing, SEM image for (b) whole fracture surface, (c) crack morphology and (d) smooth area.

Fig. 12 TEM microstructure of the SLM-1000 sample: (a) bright field image for Ti_2Ni phases at a grain boundary, SAED patterns obtained respectively from the (b) left and (c) right regions of the grain boundary shown in (a)and, and (d) bright field image for dislocations obtained under the two-beam condition inside the sample.

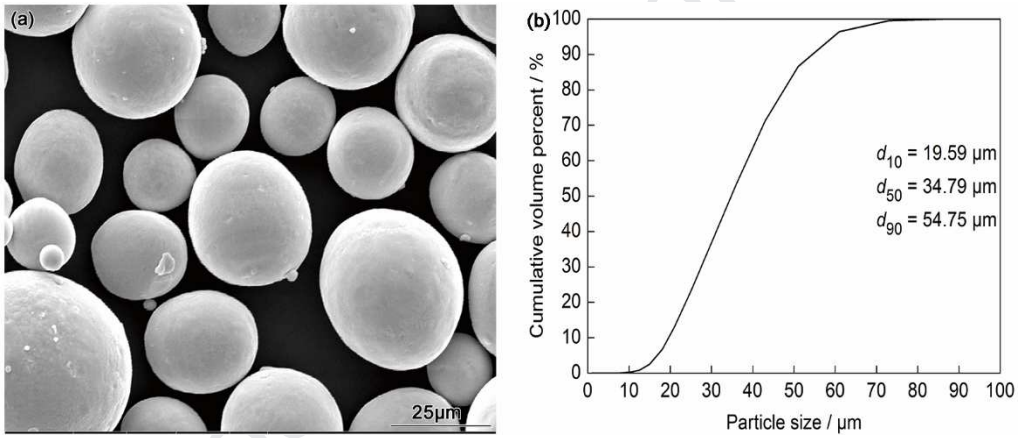

Fig. 1 (a) The SEM shape morphology and (b) the size distribution of Ti-Ni powder.

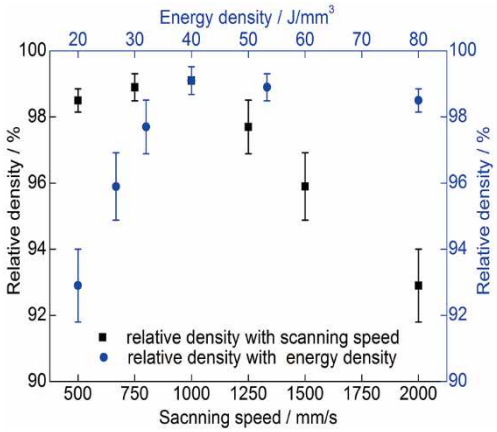

Fig. 2 The relationship between relative density of SLM Ti-Ni parts with SLM scanning speeds or input laser energy density.

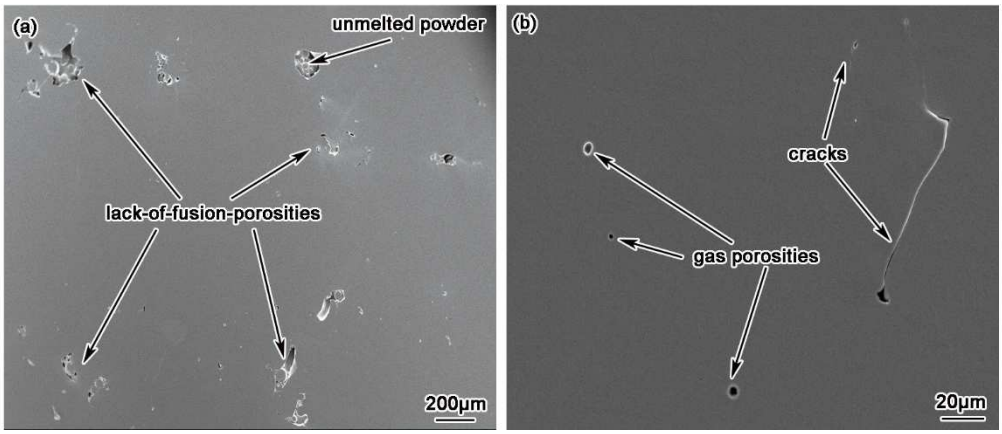

Fig. 3 The SEM images for top surface after mechanically ground and polished to show the defects of (a) SLM-1500 and (b) SLM-500.

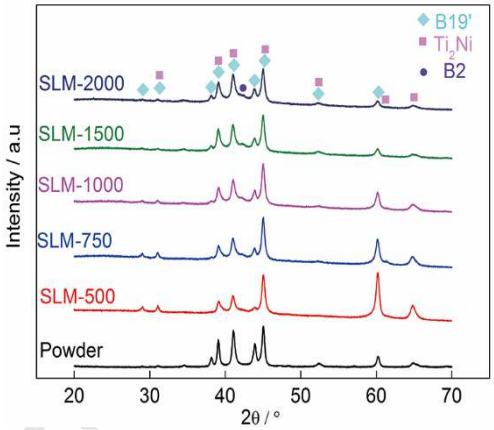

Fig. 4 The XRD spectra of the Ti-Ni powder and SLM fabricated samples at different laser scanning speeds.

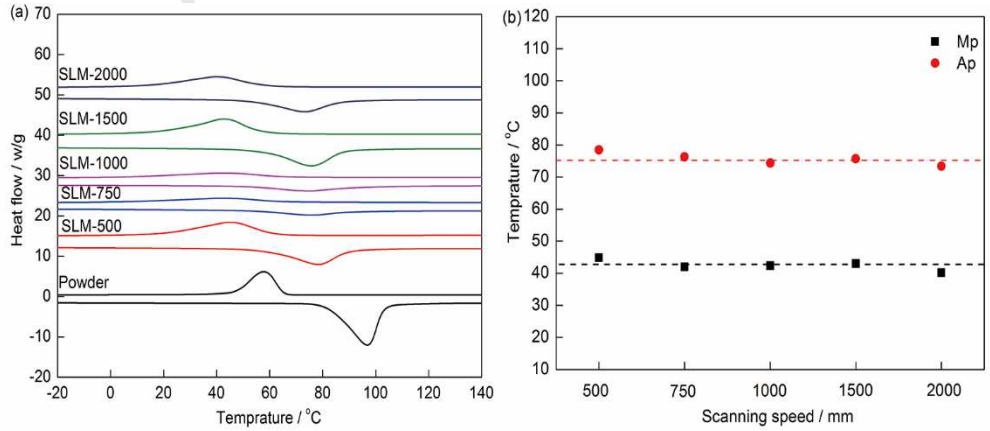

Fig. 5 (a) The DSC curves and (b) temperature of phase transformation peaks of Ti-Ni powder and SLM fabricated samples at different laser scanning speeds.

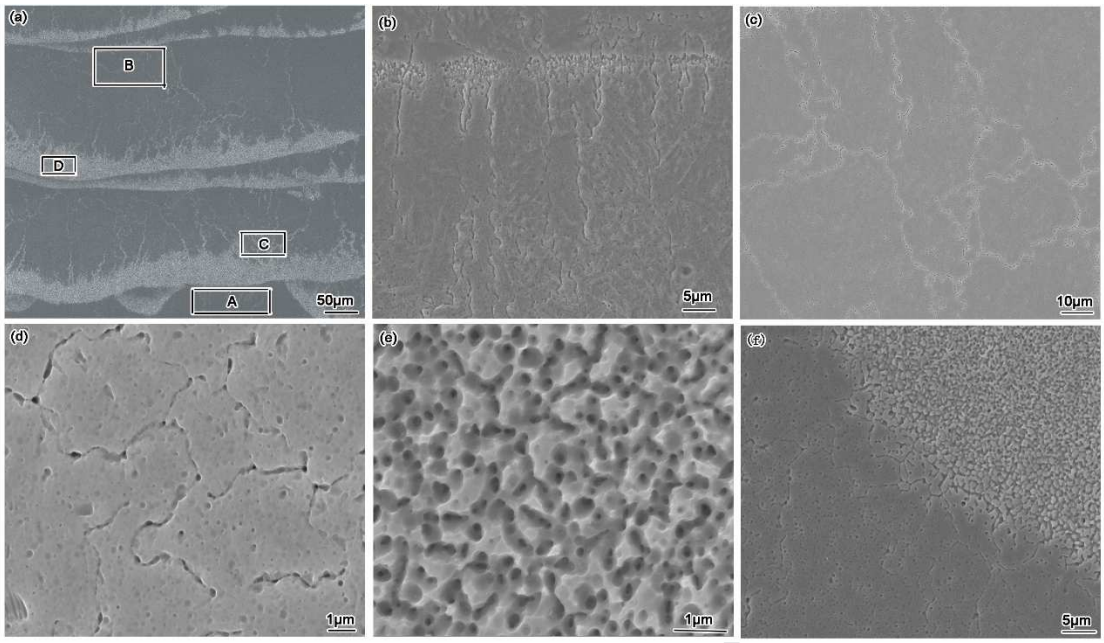

Fig. 6 The SEM microstructure of SLM-1000: (a) top surface of molten pool, (b) the area of A in Fig. 6a for columnar grains, (c) the area of B in Fig. 6a for large scale equiaxed grains,, (d) the area of C in Fig. 6a for little size equiaxed grains, (e) the area of D in Fig. 6a for nanoscal or sub-micro equiaxed grains, (f) molten pool boundary area.

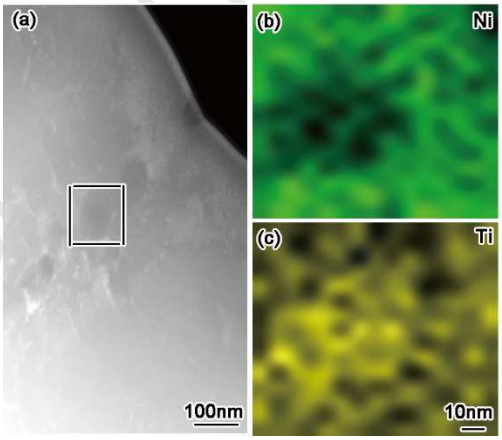

Fig.7 (a) Low-magnification STEM image of a grain boundary with precipitation phases in SLM-1000, (b) and (c) EDS results obtained from a precipitation marked in (a).

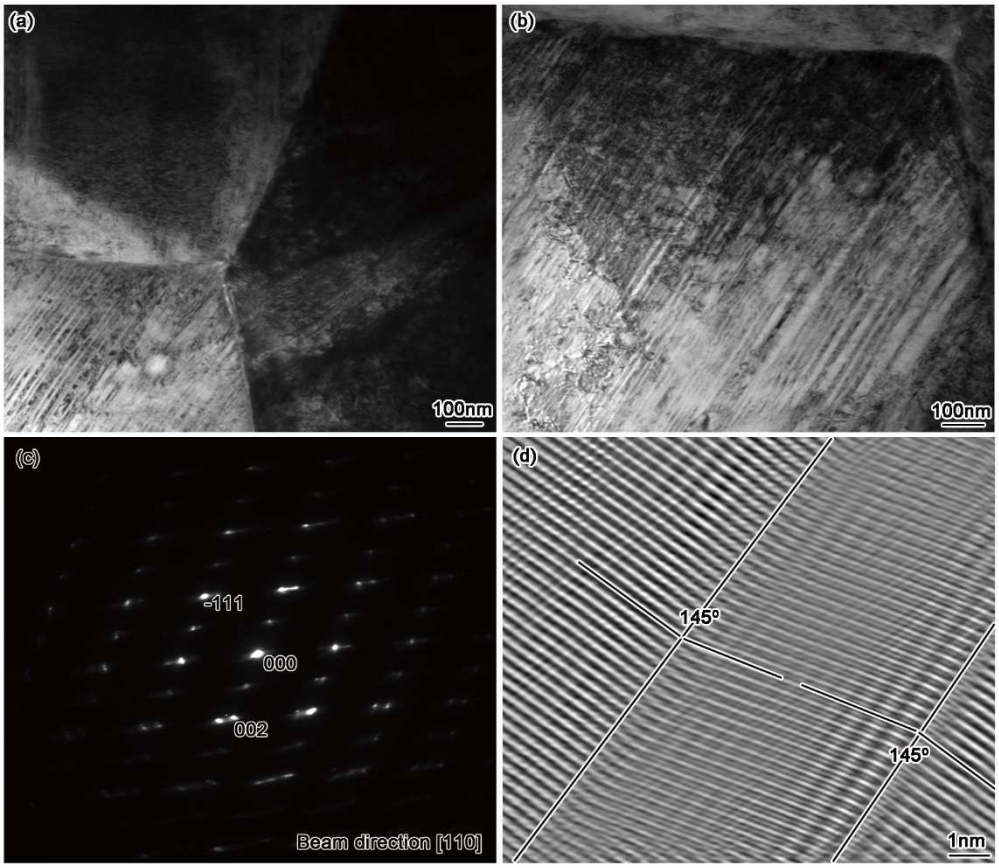

Fig. 8 TEM microstructure of SLM-1000: (a) bright field image, (b) the morphology of twins, (c) the corresponding SAED pattern obtained from the region containing twins, (d) high-resolution TEM image for a twin with the misorientation angle of 145° at the twin boundaries.

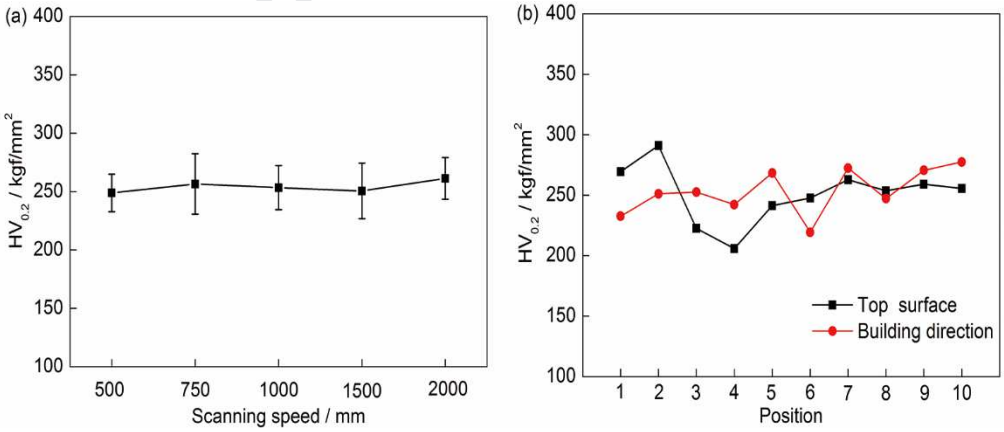

Fig. 9 The Vickers hardness of (a) SLM fabricated samples in different scanning speed and (b) SLM-1000 along the building direction and the top surface on a straight testing line that spans the entire sample for ten different positions respectively.

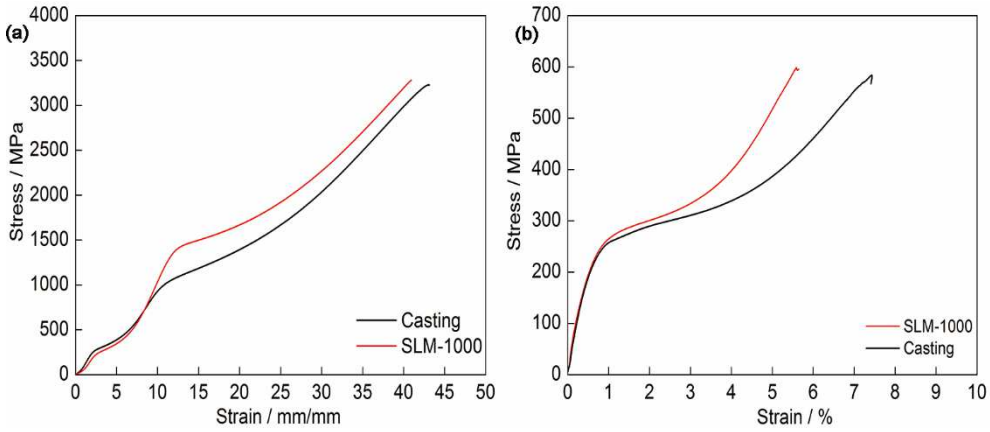

Fig. 10 The compression of (a) and tensile of (b) stress-strain curves loaded until failure for SLM-1000 and the cast counterpart with the same chemical composition.

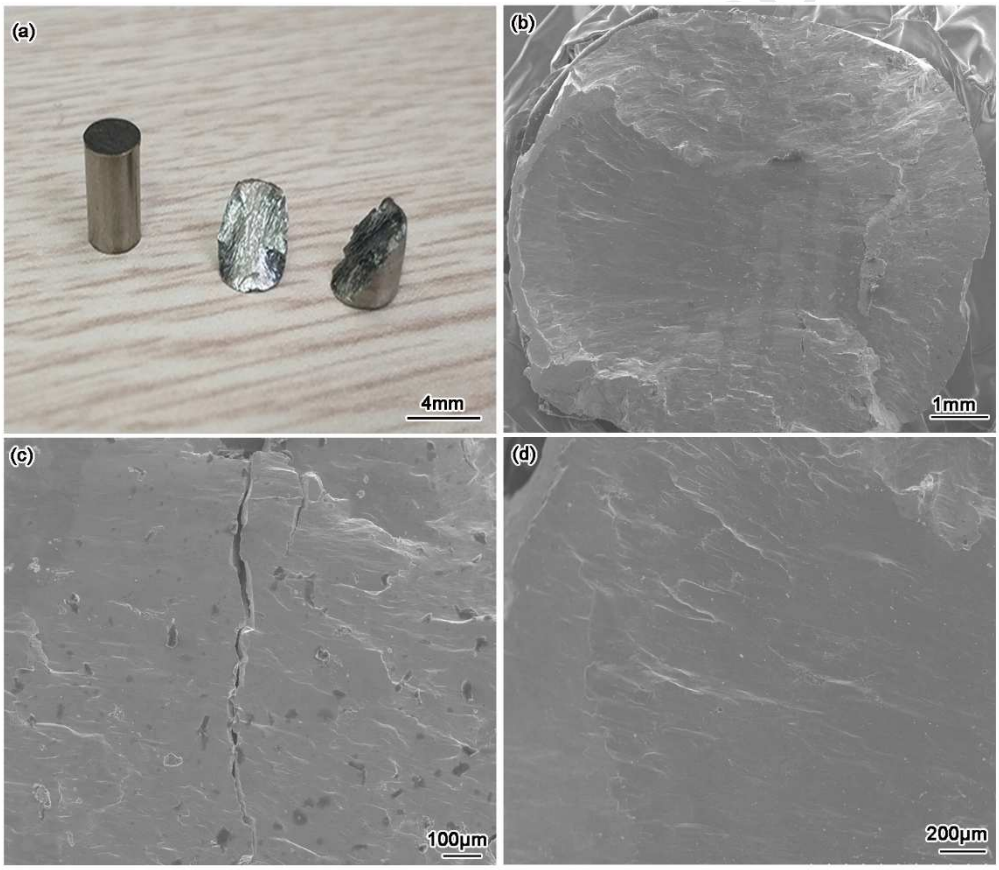

Fig. 11 (a) The morphology of SLM-1000 before and after compression testing, SEM image for (b) whole fracture surface, (c) crack morphology and (d) smooth area.

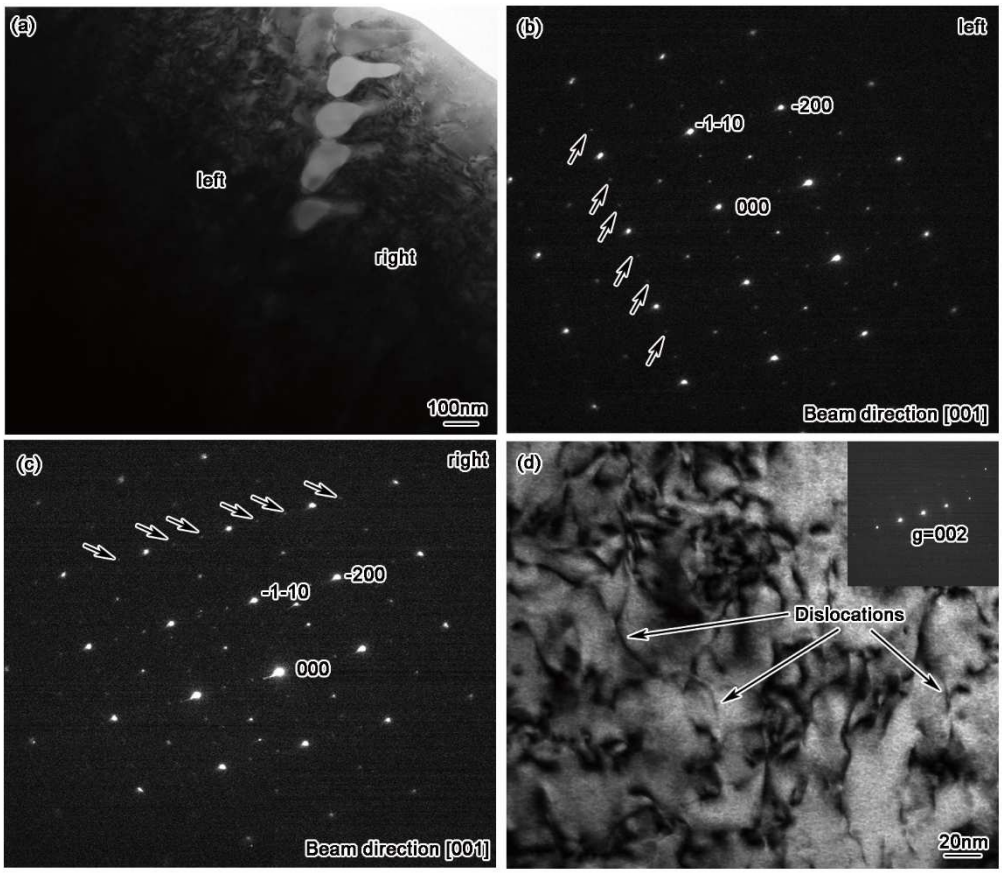

Fig. 12 TEM microstructure of the SLM-1000 sample: (a) bright field image for Ti_2Ni phases at a grain boundary, SAED patterns obtained respectively from the (b) left and (c) right regions of the grain boundary shown in (a)and, and (d) bright field image for dislocations obtained under the two-beam condition inside the sample.

Declaration of interests

The authors declare that they have no known competing financial interests or personal relationships that could have appeared to influence the work reported in this paper.